ROYAL SOCIETY
OF CHEMISTRY

PAPER

Check for updates

Multi-compositional hierarchical nanostructured Ni3S2@MoSx/NiO electrodes for enhanced electrocatalytic hydrogen generation and energy storage†

Kane Jian Hong Lim, [ab] Gamze Yilmaz, [a] Yee-Fun Lim [c] and Ghim Wei Ho [*acd]

Rational design of multi-compositional hierarchical nanostructures from earth-abundant materials holds great potential in the fields of electrocatalytic hydrogen evolution and supercapacitive energy storage. However, such nanostructures often require multi-step synthesis routes which are rather elaborate. In this study, we demonstrate a facile synthesis route to attain hierarchical nanostructures comprised of multiple constituents with varied geometric dimensionality, *i.e.* NiO nanoparticles incorporated in two-dimensional (2D) sulfurized molybdenum-based nanosheets coated on a one-dimensional (1D) Ni_3S_2 nanorod scaffold grown directly on Ni foam. The metallic nature of the Ni_3S_2 nanorods provides a 1D conductive pathway to the active sites, and their overall nanostructure increases the specific surface area of the electrode and maintains the structural integrity. Furthermore, synergistic interactions between the molybdenum-based nanosheets and NiO nanoparticles can improve the overall activity of the catalyst towards the hydrogen evolution reaction (HER) *via* playing specific roles in the water dissociation and hydrogen adsorption steps. Consequently, the design of the multi-compositional hierarchical nanostructure led to a remarkable enhancement in electrocatalytic hydrogen evolution performance, and this material also exhibited excellent supercapacitive energy storage properties. This work illustrates a straightforward approach to the design and tailoring of hierarchical nanostructured materials with promising application in the field of energy conversion and storage.

Introduction

Growing concerns regarding climate change and global carbon dioxide emissions amidst a world with continually rising energy demands have compelled us to develop clean and renewable alternatives to fossil fuels, such as through electrocatalysis[1,2] and supercapacitors.[3] Molecular hydrogen evolved through electrolysis presents itself as one such promising alternative energy carrier,[4,5] whereas supercapacitors are another modern means of energy storage.[6,7] To realize the actualization of these energy conversion and storage technologies on a large scale, the electrodes used

inevitably have to be synthesized from inexpensive noble metal-free materials.[8,9] For instance, non-noble metal sulfides, such as sulfides of nickel, cobalt, iron and molybdenum, have recently attracted much attention in the fields of energy conversion and storage (*e.g.*, electrochemical capacitors and batteries) due to their favorable electrochemical performance.[10–13] In particular, sulfide materials with heteroatoms or multiple components were employed as these hybrid catalysts exhibit enhanced activities arising from the synergistic effects between the different components.[14–19]

Among the earth-abundant sulfides, MoS_2 has garnered much interest for the electrocatalytic hydrogen evolution reaction (HER). First noticed for having active sites resembling those of natural hydrogen producing enzymes (hydrogenases and nitrogenases), the theoretical proposal and experimental verification of its exceptional edge site activity[20,21] have spurred a vast range of studies focused on developing molybdenum-based catalysts for usage in electrocatalytic hydrogen production.[22–25] Reasonably, owing to its earth abundance, relatively low cost, high active site activity and good stability, MoS_2 is a popular choice as a catalyst material.[22,24] However, the intrinsically low electronic

aDepartment of Electrical and Computer Engineering, National University of Singapore, 4 Engineering Drive 3, 117583, Singapore. E-mail: elehgw@nus.edu.sg

bNUS Graduate School for Integrative Sciences and Engineering, National University of Singapore, 28 Medical Drive, 117456, Singapore

*cInstitute of Materials Research and Engineering, A*STAR (Agency for Science, Technology and Research), 3 Research Link, 117602, Singapore*

dEngineering Science Programme, National University of Singapore, 9 Engineering Drive 1, 117575, Singapore

This journal is © The Royal Society of Chemistry 2018

J. Mater. Chem. A, 2018, 6, 20491–20499 | 20491

conductivity of molybdenum sulfide can hinder electron transport to catalytic sites resulting in poor overall catalytic activity.[23,26] Thus, one effective means researchers have since adopted is coupling of MoS_2 with a conductive scaffold, thereby enhancing electron transport to catalytic sites; such examples include MoS_2/MoO_{3-x} nanowires,[27] MoS_2 on graphene,[28–30] amorphous MoS_x on graphene/Ni foam,[31] amorphous MoS_x on carbon nanotube hybrids[32–34] and others. Likewise, supercapacitor electrodes based on sulfurized-molybdenum too suffer from a similar conductivity issue, and equivalent strategies can be applied.[35–40] Yet, such multi-compositional structures typically require elaborate synthesis routes with multiple steps to first grow the scaffold followed by deposition of active materials, which could ultimately increase the fabrication complexity and cost of the electrodes. Henceforth, a non-complex means of fabricating multi-compositional hierarchical structures with equally improved electrochemical performance would be preferred. Furthermore, the structure and composition of the scaffold would undoubtedly have to be judiciously selected in order to impart accompanying properties targeted towards improvement of performance; these can include ion trapping,[29] increment of surface area,[27,32] reduction in aggregation[28,39] and others. In general, two primary strategies can be employed to improve the performance of an electrode: (i) increasing the number of electrically accessible active sites or (ii) improving the overall activity of these active sites.

Herein, we present a multi-compositional hierarchical electrode grown through a facile one-step hydrothermal method designed from a combination of these two strategies. The catalyst was formed by a dense array of one-dimensional (1D) Ni_3S_2 nanorods coated with NiO-decorated two-dimensional (2D) MoS_x nanosheets grown directly on Ni foam. The protruding nanostructure array provided high specific surface area which correspondingly led to the appreciably increased number of active sites. Concurrently, the metallic nature of the nanorods provided a 1D conduction path to the active sites to ensure that catalysis would not be hindered by electron transport. Resultantly, the performance of these multi-compositional hierarchical nanostructures towards the HER was superior compared to that of similarly synthesized catalysts of a lower aspect ratio or with a mere coating. In addition, the synthesis process further incorporates NiO nanoparticles into the catalytically active MoS_x nanosheet layer, whose presence encourages synergistic interactions with Mo–S active sites for water dissociation, thereby enhancing the overall activity of the catalytic sites towards hydrogen evolution. The increase in the electrocatalytically active surface area of the synthesized nanostructured electrode would be beneficial not only for electrocatalytic performance but also for electrochemical energy storage. Furthermore, the rich redox chemistry of the Mo-based nanosheets makes them suitable for use as a supercapacitor. Hence, the multi-compositional hierarchical nanostructured electrode synthesized not only exhibited enhanced performance as an electrocatalyst electrode material but also exhibited remarkable electrochemical performance and stability as a supercapacitor.

Experimental section

Materials

Sodium molybdate dihydrate (Na_2MoO_4) and potassium hydroxide (KOH) were purchased from Sigma-Aldrich. Thioacetamide (TAA, C_2H_5NS) was purchased from TCI. All the chemicals were used as received without further purification.

Synthesis of Ni_3S_2@MoS_x/NiO (NM) nanostructures

The Ni_3S_2@MoS_x/NiO nanostructures were synthesized using a hydrothermal method. A piece of nickel foam (2.5 cm by 6 cm) was cleaned through successive immersion in acetone, ethanol, and deionized (DI) water under ultra-sonication for 10 min per solution, followed by blow-drying with nitrogen gas. The nickel foam was then transferred into a Teflon-lined stainless steel autoclave containing 25 mL DI water with 1 mmol thio-acetamide and varied amounts of sodium molybdate (0.125, 0.625 and 0.75 mmol were used for NM-sheets, NM-rods and NM-stubs, respectively). Subsequently, the autoclave was sealed and heated to 200 °C for 24 h. The autoclave was then allowed to cool naturally to room temperature, and the sample was removed and rinsed with excess DI water. Finally, the sample was dried in an electric oven at 55 °C.

Synthesis of Ni_3S_2 (NS) nanorods

To synthesize the NS-rods, a piece of nickel foam (2.5 cm by 6 cm) was cleaned as previously described. The nickel foam was then transferred into a Teflon-lined stainless steel autoclave containing 30 mL DI water with 4.8 mmol thioacetamide. Subsequently, the autoclave was sealed and heated to 150 °C for 16 h. The autoclave was then allowed to cool naturally to room temperature, and the sample was removed and rinsed with excess DI water. Finally, the sample was dried in an electric oven at 55 °C.

Synthesis of MoS_x-coated Ni_3S_2 nanorods

NS-rods coated with MoS_x nanosheets were grown through a secondary hydrothermal step. The NS-rod sample was placed in a Teflon-lined stainless steel autoclave containing 25 mL DI water with 1 mmol thioacetamide and 0.5 mmol sodium molybdate. Subsequently, the autoclave was sealed and heated to 200 °C for 20 h. The autoclave was then allowed to cool naturally to room temperature, and the sample was removed and rinsed with excess DI water. Finally, the sample was dried in an electric oven at 55 °C.

Characterization

Scanning electron microscope (SEM) images were taken with a JEOL JSM-7001F field emission scanning electron microscope (FESEM) equipped with an energy dispersive X-ray spectroscope (EDX), and transmission electron microscope (TEM) images were obtained using a JEOL JEM-2100 electron microscope. X-ray diffraction (XRD, D5005 Bruker X-ray diffractometer equipped with graphite-monochromated Cu Kα radiation at λ = 1.541 Å) was employed to obtain the XRD patterns of the

samples. X-ray photoelectron spectroscopy (XPS) spectra were recorded on a VG Thermo Escalab 220I-XL system, and all binding energies were referenced to the C 1s peak of 284.8 eV.

Electrochemical measurements

Hydrogen evolution reaction (HER) tests. The electrocatalysis measurements were performed on a CHI 660E electrochemical workstation, in a three-electrode configuration at 25 °C. The as-prepared substrates were used directly as the working electrode, while Pt foil and a saturated calomel electrode (SCE) were used as the counter electrode and reference electrode, respectively. All tests were conducted in an aqueous solution of 1 M KOH as the electrolyte, and the measured potentials were converted to the reversible hydrogen electrode (RHE) based on the following formula: E_{RHE} (V) = E_{SCE} (V) + 0.242 + 0.059 × pH. Linear sweep voltammetry (LSV) curves were measured at a scan rate of 5 mV s^{-1}. Electrochemical impedance spectra (EIS) were recorded in the frequency range of 0.01 Hz to 100 kHz with 5 mV amplitude at an overpotential of 100 mV. Cyclic voltammetry (CV) was conducted at various scan rates from 5 mV s^{-1} to 150 mV s^{-1} in the potential window where no redox peaks were observed (0.05 V to 0.15 V *versus* RHE). The current density differences were calculated at 0.1 V and used to evaluate the capacitance values. The current density *versus* time (*I–t*) curve was recorded at an overpotential of 125 mV for 50 h.

Supercapacitor tests. The electrochemical properties of NM-rods were examined in a three-electrode configuration at 25 °C using the as-prepared substrates directly as the working electrode, a saturated calomel electrode (SCE) as the reference electrode and Pt foil as the counter electrode in 6 M aqueous KOH electrolyte. All electrochemical measurements (cyclic voltammetry and galvanostatic charge–discharge) were conducted on a CHI 660E electrochemical workstation. The cyclic voltammetry and galvanostatic discharge profiles were obtained in a 0 V to 0.5 V potential window. The cycling stability test was performed by galvanostatically charging and discharging for 5000 consecutive cycles at 50 mA cm^{-2}.

Results and discussion

The synthesis of various MoS$_x$-coated hierarchical nanostructures on a nickel foam substrate was achieved through a facile one-step hydrothermal method, as illustrated in Fig. 1. In short, a nickel foam substrate was placed in a Teflon-lined autoclave containing an aqueous solution of thioacetamide (TAA) and sodium molybdate (Na$_2$MoO$_4$), and was heated at 200 °C for 24 h. Decomposition of TAA during the hydrothermal process released active S^{2-} ions, which reacted with the exposed nickel foam to form Ni$_3$S$_2$ nanoparticles.[41] Over time, these nanoparticles form a scaffold for the attachment of MoS$_x$ nanosheets, grown through the reaction between the S species and MoO$_4^{2-}$ ions in the solution. Additionally, Ni ions in the solution were incorporated into these nanosheets during the growth process resulting in the decoration of the nanosheets with NiO nanoparticles. Such a method of direct growth on
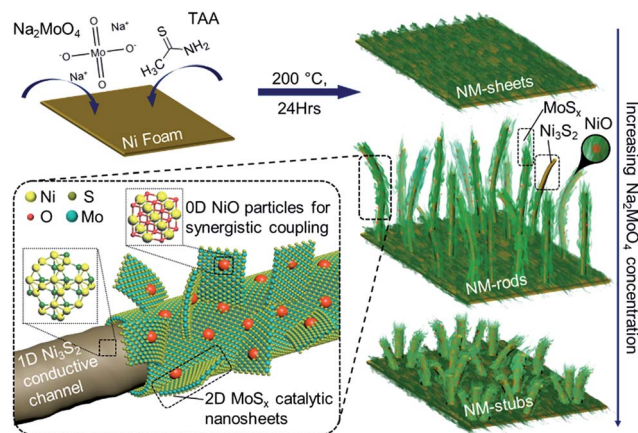

Fig. 1 Schematic diagram illustrating the synthesis process of NM-sheets, NM-rods and NM-stubs.

nickel foam allows it to serve two vital roles: (i) providing the Ni ions necessary for the growth of both the NiO nanoparticles and Ni$_3$S$_2$ structures and (ii) simultaneously acting as a substrate for the growth of the catalyst, resulting in superior interfacial contact between the electrode and catalyst without the need for a binder and thereby enhancing the electrical conductance to the catalyst.[42] Resultantly, NiO-decorated MoS$_x$ nanosheet-coated Ni$_3$S$_2$ hierarchical structures were obtained, the morphology of which could be selectively altered between sheet-like, long rod-like and short stub-like by varying the concentration of the Mo-precursor in the growth solution (Fig. 1). From a structural design point of view, dense structures with high aspect ratios are generally more favorable for electrochemical reactions by virtue of their increased specific surface area, which consequently leads to a corresponding increase in the density of active sites. Thus, it can be hypothesized that the long rod-like sample would be most ideal among the synthesized nanostructures for electrocatalysis.

The MoS$_x$-coated Ni$_3$S$_2$ nanorod structure was characterized using scanning electron microscopy (SEM), and the results are shown in Fig. 2a–c. The sample showed long thin Ni$_3$S$_2$ nanorods protruding from the surface of the Ni-foam (Fig. 2b). These nanorods were found to have an approximate length of 3 μm and grew with good density and surface coverage (Fig. 2a). The individual nanorod structures were also observed to be covered by MoS$_x$ nanosheets (Fig. 2c), and this sample would be denoted as NM-rods. SEM-EDX mapping performed on an individual broken-off rod (Fig. S1†) revealed its elemental composition to consist of elements Ni, O, S and Mo. The distribution of Ni was found to be concentrated heavily at the central core while the surrounding sheets consist mostly of S and Mo with a low content of Ni.

Other MoS$_x$-coated Ni$_3$S$_2$ hierarchical structures synthesized through varying the Mo-precursor concentrations were also characterized using SEM (Fig. 2d and e). Samples synthesized in a low molybdenum environment (Fig. 2d) exhibited the rough surface texture of the sulfurized nickel foam covered by layers of nanosheets with no apparent protrusions and would be denoted as NM-sheets, while, addition of the Mo-precursor in excess
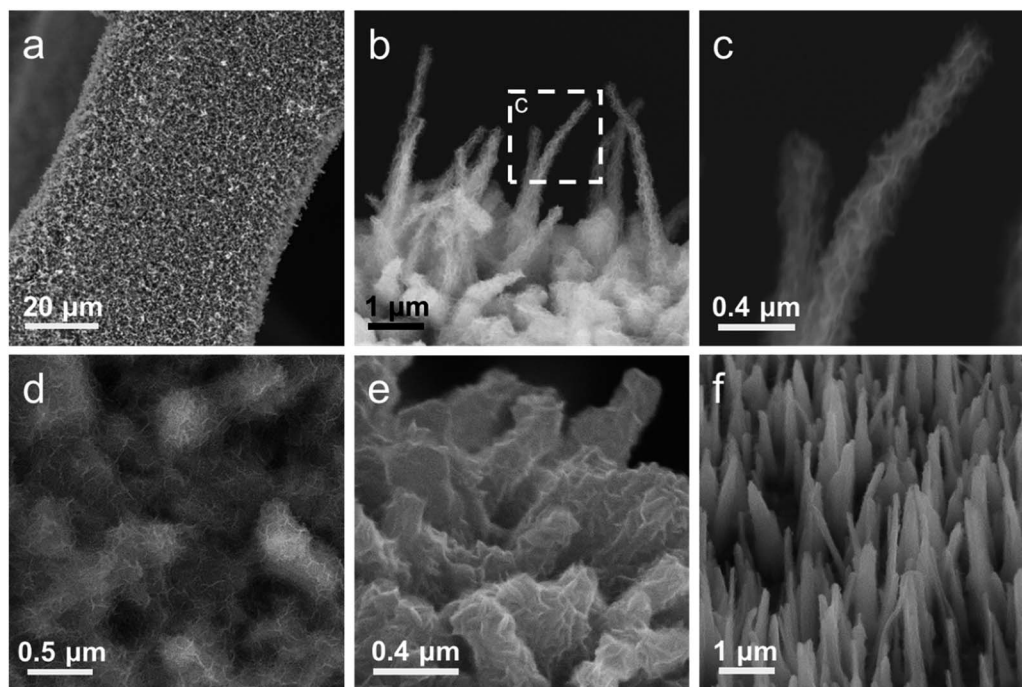
Fig. 2 (a) Low-magnification SEM image of NM-rods. High-magnification SEM images of (b and c) NM-rods, (d) NM-sheets, (e) NM-stubs and (f) Ni_3S_2 nano-rods (NS-rods).

(Fig. 2e) resulted in rods with an increased diameter, albeit at a compromise of reduced length. As compared to the NM-rods, these structures were short and stub-like in nature, and would be denoted as NM-stubs. Additionally, hydrothermally grown pristine Ni_3S_2 nanorods (NS-rods) without Mo-precursors were also synthesized (Fig. 2f), as a control sample. The sample was composed of thin nanorods identical to the NM-rod sample but without the MoS_x nanosheet layer. The chemical composition and phase of the sample were confirmed using SEM-EDX and X-ray diffraction (XRD) analysis, respectively, and was found to consist purely of Ni_3S_2 rods (Fig. S2†), similar to the core of NM-rods.

Transmission electron microscopy (TEM) imaging of a typical NM-rod (Fig. 3a) showed that the rod comprises of a central core coated with 2D nanosheets. These nanosheets were well extended outwards from the core structure and exhibited a highly porous nature (Fig. 3b and c). Such an extension of the nanosheets in conjunction with their porous nature is beneficial for electrochemical reactions due to the increased ease at which reactants may diffuse to an active site, thus enhancing its mass transport. Interestingly, the TEM images also revealed the presence of nanoparticles decorating the nanosheets (Fig. 3b). Through high resolution TEM (HRTEM) imaging (Fig. 3d and e) of these nanoparticles, lattice fringes with an interplanar spacing of 0.21 nm and 0.24 nm were observed and can be assigned to the (200) and (111) planes of NiO, respectively.[43,44] The presence of such NiO nanoparticles can enhance the electrocatalytic activity of the electrode through synergistic interactions beneficial for the HER.[45,46] Separately, similar HRTEM imaging (Fig. 3f) of the core of the rod showed lattice fringes with an interplanar spacing of 0.4 nm

which can be assigned to the (101) plane of Ni_3S_2.[45] Consequently, HRTEM imaging at the tip of the nanorod (Fig. 3d, the area inside the dashed square in Fig. 3a) exhibits two sets of lattice patterns, corresponding to NiO and Ni_3S_2, and the amorphous nanosheet layer indicating that the sample evidently comprises three distinct components.

The material microstructure of NM-rods was further investigated through XRD (Fig. 4a). Apart from the strong signals at 44.6°, 51.9°, and 76.3° which could be indexed to the (111), (200), and (220) signals from the nickel foam substrate, respectively (JCPDS no. 65-2865),[41,47] additional signals positioned at 21.7°, 31.1°, 37.8°, 49.7°, and 55.2° were observed in the XRD pattern and correspond to the (101), (110), (003), (113), and (122) signals from single crystalline Ni_3S_2, respectively (JCPDS no. 44-1418).[41,47] The absence of signals related to MoS_x species in the XRD pattern was however noted, possibly due to the thin film and amorphous nature of the nanosheets. In addition, SEM-EDX spectral analysis of the sample (Fig. 4b) acknowledges the presence of Mo and S-species, yet the similar X-ray emission peak positions of Mo and S make differentiating the individual elements difficult. Thus, the SEM-EDX results were further corroborated by performing X-ray photoemission spectroscopy (XPS) to clearly show the presence of Mo and S species (Fig. 4c). A high resolution XPS scan in the Mo 3d region was recorded on the NM-rod sample (Fig. 4d), and the spectrum revealed two sets of doublet peaks at 234.3 and 231.1 eV which could be attributed to Mo^{4+},[32] and 235.6 and 232.4 eV which were attributed to Mo^{6+},[48] in addition to an S 2s peak at 226.0 eV.[31,49] The existence of multi-valence states along with broad peaks suggests that the as-grown material resembles amorphous MoS_x.[32] In contrast, no Mo peaks were observed in
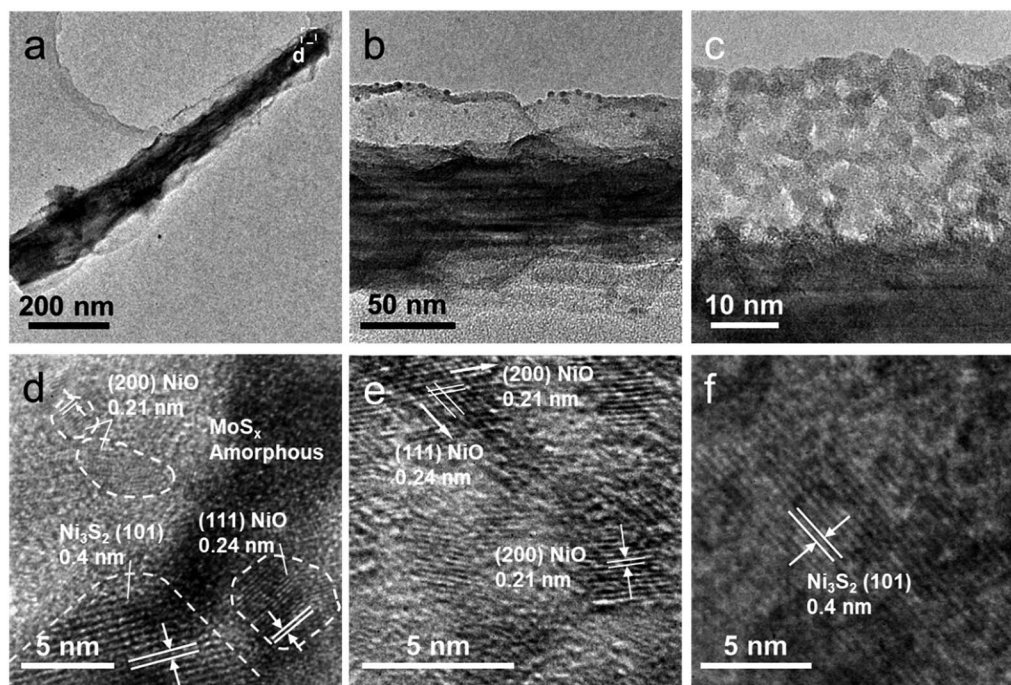
20494 | J. Mater. Chem. A, 2018, 6, 20491–20499

This journal is © The Royal Society of Chemistry 2018

Fig. 3 (a–c) Low-resolution TEM images of NM-rods and (d–f) high-resolution TEM images showing the presence of (e) NiO and (f) Ni_3S_2.

this region of the spectrum of the NS-rod control sample (Fig. S3†). The XPS spectrum of the S 2p region (Fig. 4e) could be fitted with peaks of S $2p_{1/2}$ and S $2p_{3/2}$ at energies of 163.0 and 161.7 eV, respectively,[48] while the peak at 168.6 eV is most likely associated with surface oxidized S species[50] possibly due to the presence of oxidative molybdenum species, synthesis through aqueous routes and exposure of the sample to air.[50] Although the presence of surface oxidation would presumably have

a definite impact on the catalyst, some have proposed that such an oxidation could lead to the generation of active surface sites for the HER.[50] Lastly, the characteristic peaks of Ni $2p_{1/2}$ and Ni $2p_{3/2}$ were found at 873.4 and 855.9 eV accompanied by their respective satellite peaks at 879.1 and 861.6 eV (Fig. 4f). This is indicative of the presence of oxidized Ni species,[47] which reasonably exists in the form of NiO. Additionally, the peak at 853.6 eV corresponds to the characteristic peak of Ni_3S_2.[47,51]
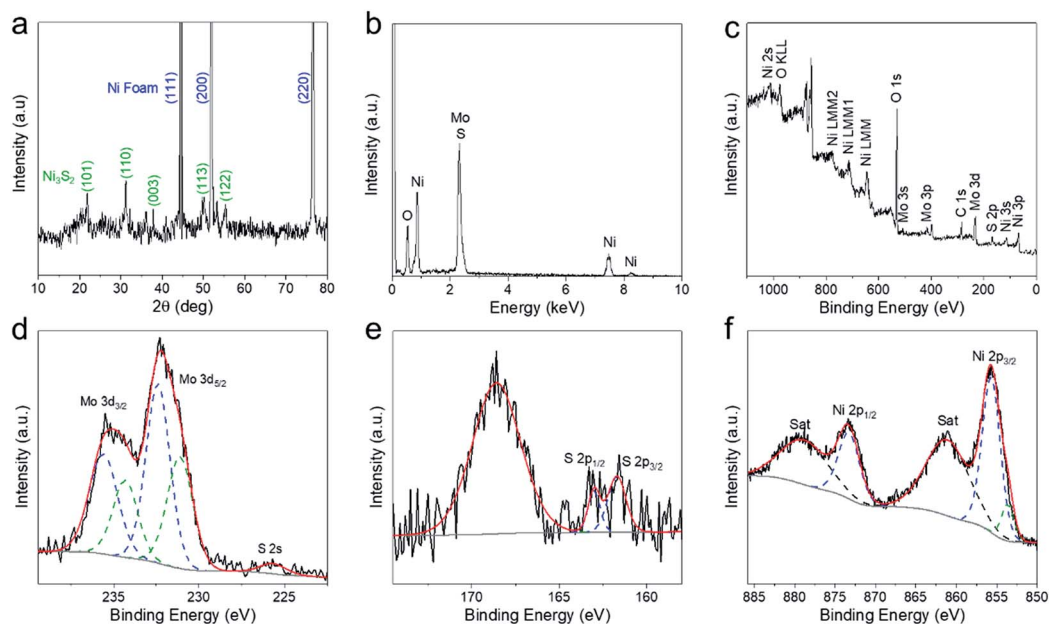

Fig. 4 (a) XRD spectrum of NM-rods. (b) SEM-EDX spectrum of NM-rods. (c) XPS survey scan of NM-rods and XPS high resolution scans in (d) Mo 3d, (e) S 2p and (f) Ni 2p regions.

This journal is © The Royal Society of Chemistry 2018

J. Mater. Chem. A, 2018, **6**, 20491–20499 | **20495**

Following this, the electrocatalytic activities of the NM-sheets, NM-rods, NM-stubs and NS-rods for the HER were studied in alkaline media (1 M KOH). The as-synthesized products grown on the nickel foam substrate were directly used as the working electrode to obtain the polarization curves shown in Fig. 5a and the corresponding Tafel plots in Fig. 5b. Among the four electrodes, NM-rods exhibited the best catalytic performance giving a much higher geometrical current density (J) at the same overpotential. Notably, the NM-rods only required an overpotential of 118 mV to attain $J = 10$ mA cm^{-2}, which was substantially lower compared to the 151 mV and 177 mV needed for NM-stubs and NM-sheets, respectively (Fig. 5c). Unsurprisingly, the corresponding Tafel slopes followed a similar trend, with results of 65 mV dec^{-1} for NM-rods being lower than the 71 mV dec^{-1} and 86 mV dec^{-1} for NM-stubs and NM-sheets, respectively. On the other hand, NS-rods with no MoS$_x$ nanosheets performed significantly worse compared to the MoS$_x$-coated samples. To attain a current density of $J = 10$ mA cm^{-2}, the electrode required an overpotential of 309 mV and had a corresponding Tafel slope of 123 mV dec^{-1}. However, when the NS-rods undergo a secondary growth step to coat a layer of sulfurized Mo-based nanosheets, they showed a significant improvement in the overpotential to 140 mV (Fig. S4†). Therefore, these results further substantiate the importance of the MoS$_x$ nanosheet layer as an essential component for an effective electrocatalyst material system. Although the amorphous MoS$_x$ nanosheets do not possess well-defined edge sites compared to crystalline MoS$_2$, their amorphous nature allows them to possess an abundance of defect sites which comprises of coordinatively unsaturated sulfur atoms. These unsaturated sulfur atoms act as adsorption sites for hydrogen atoms, which eventually leads to hydrogen evolution.[52,53]

To further investigate the superior performance of NM-rods over the other electrodes, additional electrical characterization was carried out. Firstly, the electrochemically active surface area (ECSA) values of the various electrodes were compared through measuring their double layer capacitance (C_{dl}) in a non-faradaic region at different scan rates. This measurement gives an indication of the number of active sites in the catalyst, which is one of the important factors in determining its performance. The results, as shown in Fig. 5d, show the calculated capacitances of 312 mF cm^{-1}, 189 mF cm^{-1} and 38 mF cm^{-1} obtained for NM-rods, NM-stubs and NM-sheets, respectively, whereby the higher capacitive performance of NM-rods is indicative of a greater number of electroactive sites within the sample. One possible reason for this comparatively larger number of active sites in NM-rods could be attributed to the higher aspect ratio of their nanostructure which leads to a higher specific surface area and by extension, more active sites. Furthermore, the presence of porous nanosheets which extend out from the rods into the solution would further increase the number of active sites available for the reaction. Thus, unsurprisingly, the NS-rods without these porous active nanosheets only managed to exhibit a comparatively much lower value of 3 mF cm^{-1}. Subsequently, electrochemical impedance spectroscopy (EIS) measurements were also carried out to evaluate the charge transfer kinetics of the electrodes (Fig. 5e). These measurements further corroborate the good performance of NM-rods which showed the least charge-transfer resistance (R_{ct}) among the tested electrodes, and this is indicative of a relatively lower diffusion resistance of the sample.
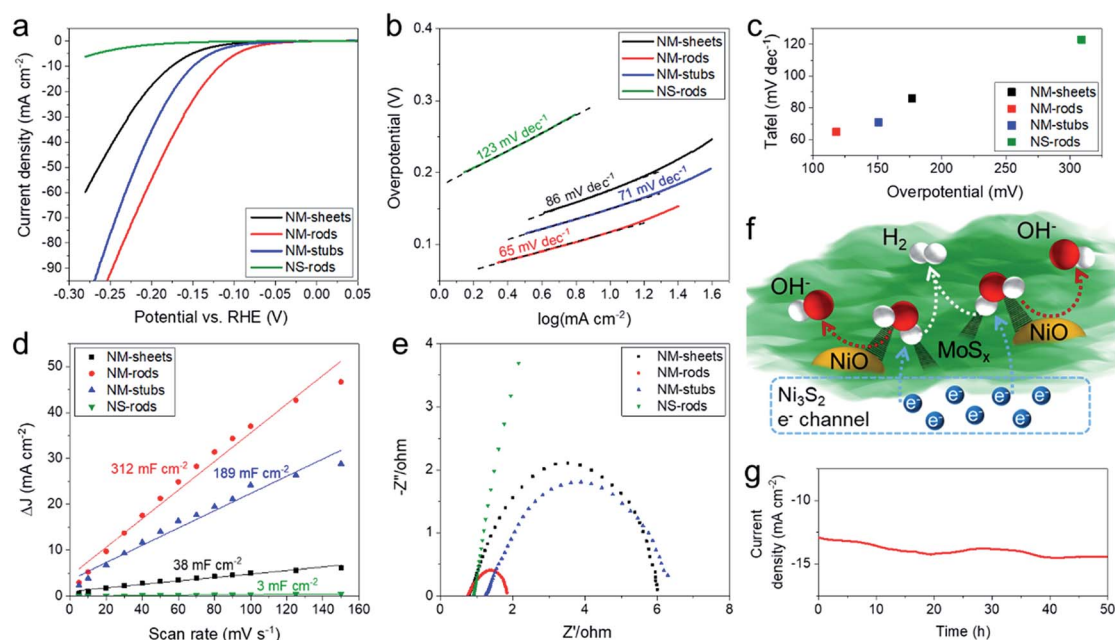

Fig. 5 (a) Polarization curves at a scan rate of 5 mV s^{-1}, (b) the corresponding Tafel plot and (c) comparison of the Tafel slope against overpotential at $J = 10$ mA cm^{-2} of the synthesized products. (d) Electrochemically active surface area measurement results and (e) electrochemical impedance measurement results of the synthesized products. (f) Schematic representation of H$_2$ production aided by NiO. (g) Stability of NM-rods at overpotential of 125 mV.

Apart from the increased specific surface area provided by the high aspect ratio nature of the NM-rod core structure, these Ni_3S_2 rods, which are of metallic nature,[54] also possess another important role of conducting electrons to the active sites. Due to the anisotropic conductivities of MoS_2, its limited conductivity along certain crystallographic directions could hinder charge transportation within the material.[27] However, in this aspect, NM-rods circumvent this issue through coupling of the catalytically active MoS_x sheets to a conductive Ni_3S_2 core. Therefore, the core provides an efficient 1D conduction path, which improves charge transport to the active sites. It would also be timely at this juncture to discuss the effect of NiO nanoparticles found on the sample for electrocatalytic activity. For the HER in an alkaline medium, it has been previously put forth that additional energy is needed for water dissociation prior to proton absorption and is therefore a contributing factor in determining overall HER activity.[55,56] In this regard, the presence of NiO nanoparticles decorated along and within the MoS_x nanosheet layers can function as an active component to facilitate water dissociation thereby enhancing the overall activity of the catalyst, as schematically depicted in Fig. 5f. NiO inherently has a lower OH^- chemisorption free energy and is capable of promoting the favorable attachment of OH^- to its surface.[45,46] Concurrently, the remaining H^+ from the dissociation of water would be able to preferentially attach to a nearby Mo–S edge site, forming the reaction intermediate for eventual hydrogen production. By considering the reaction pathways for the HER in alkaline media, it is widely accepted that water has to be dissociated first through an initial Volmer step before subsequent generation and release of molecular hydrogen in either the Heyrovsky or Tafel steps.[55,56] Thus, through lowering the barrier for water dissociation, this synergistic interaction can possibly lead to an enhancement of the overall electrocatalytic activity.

Finally, having assessed the activity of the catalyst, its stability is another major factor to be evaluated. Thus, the current density of NM-rods, which had the best activity, was evaluated at a constant overpotential of 125 mV over a period of 50 h. As shown in Fig. 5g, negligible change of current density was observed over the 50 h period of the measurement confirming the stability of the catalyst. In addition, the initial morphology of the sample was found to be well retained after 50 h of testing (Fig. S5a and b†), and XRD spectra (Fig. S5c†) of the sample after the stability study exhibited no changes in the material's crystal structure.

Several characteristic features of NM-rods make them a potentially suitable candidate as a supercapacitor electrode material. These features include the following: (i) sulfides are superior faradaic electrode materials compared to their corresponding oxide/hydroxide counterparts owing to better electrical conductivities and higher electrochemical activities;[57,58] (ii) bimetallic sulfides offer unique electrochemical properties by combining dissimilar redox reactivity properties of individual monometallic sulfides; (iii) molybdenum possesses a wide range of oxidation states from +2 to +6, and therefore it offers rich redox reactions;[59] (iv) recently, it was shown that amorphous MoS_2 exhibits promising supercapacitor performance (*e.g.* high

specific capacitance and good cycling stability), which is better than that of crystalline MoS_2 due to its isotropic-disordered structure that provides richer active sites and diffusion pathways for ions (*e.g.* OH^-);[59] (v) Ni_3S_2, an abundant electrode material, exhibits high theoretical specific capacity and good electrical conductivity; (vi) the 2D thin nanosheet structure introduces a large number of electrochemically active surface sites (Fig. 5d), (vii) the highly conductive nickel foam substrate can ensure fast charge transport; (viii) the binder-free NM-rod electrode helps in the effective utilization of the active materials by eliminating the "dead" volume problem caused by polymer binders. Considering the aforementioned merits, which could endow NM-rods with high specific capacitance and electrochemical stability, the performance of NM-rods as a supercapacitor electrode was investigated. Fig. 6a shows the cyclic voltammetry (CV) curves of NM-rods at various scan rates in 6 M KOH electrolyte within a potential window of 0–0.5 V. All the CV curves exhibit a couple of distinct redox peaks, revealing a faradaic process-based capacitance development related to M–S and M–S–OH (M refers to Ni or Mo) formation in the course of the electrochemical process. In general, the CV curves retained their shape at higher scan rates, whereas the redox peak potentials are shifted to more positive and negative values in oxidation and reduction regions, respectively, indicating a typical internal diffusion resistance influence at increasing scan rates. The specific capacitance of NM-rods can be calculated using the following equation:

$$C = i \times \Delta t / A \times \Delta V \quad (1)$$

where, C ($F\ cm^{-2}$) is the areal specific capacitance, i (A) is the discharge current, Δt (s) is the discharge time, A (cm^2) is the
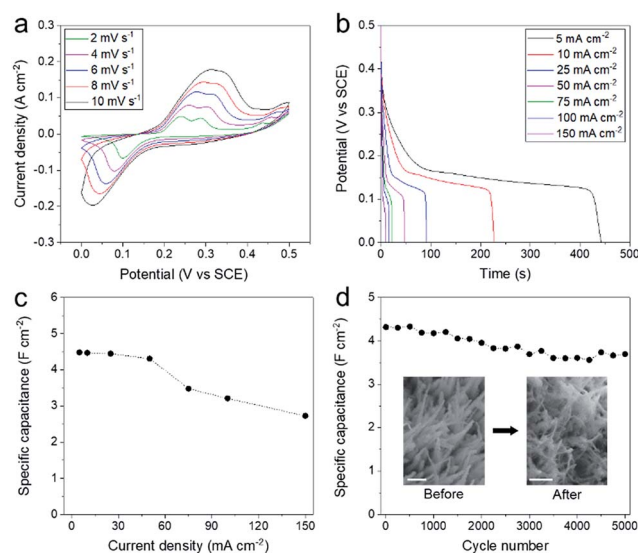

Fig. 6 (a) Cyclic voltammograms of NM-rods at scan rates of 2, 4, 6, 8 and 10 mV s^{-1}. (b) Discharge curves of NM-rods at current densities of 5, 10, 25, 50, 75, 100, and 150 mA cm^{-2}. (c) Specific capacitances of NM-rods as a function of discharge current density. (d) Cycling stability of NM-rods for 5000 cycles at a current density of 50 mA cm^{-2}. Inset: SEM images of the sample before and after the stability test, scale bar 1 μm.

This journal is © The Royal Society of Chemistry 2018

J. Mater. Chem. A, 2018, **6**, 20491–20499 | **20497**

area of the electrode material and ΔV (V) is the discharge potential window. The discharge properties required in eqn (1) (Δt and ΔV) were determined by carrying out galvanostatic discharge measurements. Fig. 6b shows the galvanostatic discharge profiles of NM-rods at various current densities ranging from 5 to 150 mA cm^{-2}. Specific capacitances at the corresponding discharge current densities were calculated using eqn (1), and the results are presented in Fig. 6c. At discharge current densities of 5, 10, 25, 50, 75, 100 and 150 mA cm^{-2}, the specific capacitances of NM-rods are 4.48, 4.47, 4.44, 4.30, 3.47, 3.20 and 2.72 F cm^{-2}, respectively. Notably, the NM-rod electrode shows excellent rate capability since it could exhibit a high specific capacitance (2.72 F cm^{-2}) even at the highest current density (150 mA cm^{-2}), that is 60% of the specific capacitance obtained at the lowest applied current density (5 mA cm^{-2}). Moreover, to ensure the robustness of the NM-rod electrode for long-term usage, the cycling stability test was carried out by performing 5000 consecutive charge–discharge cycles at a current density of 50 mA cm^{-2} (Fig. 6d). The NM-rod electrode retains 85% of its initial capacitance after 5000 cycles, indicating its excellent cyclability characteristic. Furthermore, the morphology of this electrode is well retained after testing, indicating the structural robustness of the electrode.

Conclusions

In summary, a facile one-step hydrothermal method was used to synthesize a multi-compositional hierarchical nanostructured electrode composed of Ni_3S_2 nanorod structures coated with porous MoS_x nanosheets along with decoration of NiO nanoparticles. The scaffold nanorod structure endowed the sample with an increased specific surface area, while its conductive Ni_3S_2 core ensures efficient electron transport towards the active sites. In addition, not only were the coated nanosheets able to aid further increase in the mass transport, but the synergistic interaction between the nanoparticles and nanosheets could possibly increase the overall HER activity of the catalyst. Resultantly, the NM-rod structures showed suitability for electrochemical applications, where they exhibited excellent performance in both the evolution of hydrogen through an electrocatalytic reaction and as a supercapacitor electrode for energy storage. In general, the strategies demonstrated in this study could potentially pave the way for the development of other multi-compositional hierarchical nanostructures which have been expected to be applicable as future materials in the fields of energy conversion and storage.

Conflicts of interest

There are no conflicts of interest to declare.

Acknowledgements

Notes and references

1 J. Wang, F. Tan Chuan, T. Zhu and W. Ho Ghim, *Angew. Chem., Int. Ed.*, 2016, **55**, 10326–10330.
2 W. Y. Lim, Y. F. Lim and G. W. Ho, *J. Mater. Chem. A*, 2017, **5**, 919–924.
3 G. Yilmaz, M. Yam Kah, C. Zhang, J. Fan Hong and W. Ho Ghim, *Adv. Mater.*, 2017, **29**, 1606814.
4 J. A. Turner, *Science*, 2004, **305**, 972.
5 G. Yilmaz, F. Tan Chuan, M. Hong and W. Ho Ghim, *Adv. Funct. Mater.*, 2018, **28**, 1704177.
6 J. R. Miller and P. Simon, *Science*, 2008, **321**, 651.
7 J. Liu, J. Wang, C. Xu, H. Jiang, C. Li, L. Zhang, J. Lin and Z. X. Shen, *Adv. Sci.*, 2018, **5**, 1700322.
8 I. Roger, M. A. Shipman and M. D. Symes, *Nat. Rev. Chem.*, 2017, **1**, 0003.
9 M. Q. Yang, J. Wang, H. Wu and W. Ho Ghim, *Small*, 2018, 1703323.
10 Z. Deng, H. Jiang, Y. Hu, Y. Liu, L. Zhang, H. Liu and C. Li, *Adv. Mater.*, 2017, **29**, 1603020.
11 Z. Sun, H. Lin, F. Zhang, X. Yang, H. Jiang, Q. Wang and F. Qu, *J. Mater. Chem. A*, 2018, **6**, 14956–14966.
12 Y. Guo, J. Tang, H. Qian, Z. Wang and Y. Yamauchi, *Chem. Mater.*, 2017, **29**, 5566–5573.
13 Y. Li, J. Yin, L. An, M. Lu, K. Sun, Y.-Q. Zhao, D. Gao, F. Cheng and P. Xi, *Small*, 2018, **14**, 1801070.
14 Y. Wu, Y. Liu, G.-D. Li, X. Zou, X. Lian, D. Wang, L. Sun, T. Asefa and X. Zou, *Nano Energy*, 2017, **35**, 161–170.
15 Y. Guo, J. Tang, Z. Wang, Y.-M. Kang, Y. Bando and Y. Yamauchi, *Nano Energy*, 2018, **47**, 494–502.
16 L. Yang, L. Xie, X. Ren, Z. Wang, Z. Liu, G. Du, A. M. Asiri, Y. Yao and X. Sun, *Chem. Commun.*, 2018, **54**, 78–81.
17 L. Jin, B. Liu, Y. Wu, S. Thanneeru and J. He, *ACS Appl. Mater. Interfaces*, 2017, **9**, 36837–36848.
18 L. Su, L. Gao, Q. Du, L. Hou, X. Yin, M. Feng, W. Yang, Z. Ma and G. Shao, *ACS Sustainable Chem. Eng.*, 2017, **5**, 9945–9954.
19 X. Wang, Q. Zhang, J. Sun, Z. Zhou, Q. Li, B. He, J. Zhao, W. Lu, C.-p. Wong and Y. Yao, *J. Mater. Chem. A*, 2018, **6**, 8030–8038.
20 T. F. Jaramillo, K. P. Jørgensen, J. Bonde, J. H. Nielsen, S. Horch and I. Chorkendorff, *Science*, 2007, **317**, 100–102.
21 B. Hinnemann, P. G. Moses, J. Bonde, K. P. Jørgensen, J. H. Nielsen, S. Horch, I. Chorkendorff and J. K. Nørskov, *J. Am. Chem. Soc.*, 2005, **127**, 5308–5309.
22 Q. Ding, B. Song, P. Xu and S. Jin, *Chem*, 2016, **1**, 699–726.
23 S. Jayabal, G. Saranya, J. Wu, Y. Liu, D. Geng and X. Meng, *J. Mater. Chem. A*, 2017, **5**, 24540–24563.
24 J. D. Benck, T. R. Hellstern, J. Kibsgaard, P. Chakthranont and T. F. Jaramillo, *ACS Catal.*, 2014, **4**, 3957–3971.
25 L. Chen, H. Jiang, H. Jiang, H. Zhang, S. Guo, Y. Hu and C. Li, *Adv. Energy Mater.*, 2017, **7**, 1602782.
26 Z. He and W. Que, *Applied Materials Today*, 2016, **3**, 23–56.
27 Z. Chen, D. Cummins, B. N. Reinecke, E. Clark, M. K. Sunkara and T. F. Jaramillo, *Nano Lett.*, 2011, **11**, 4168–4175.
28 Y. Li, H. Wang, L. Xie, Y. Liang, G. Hong and H. Dai, *J. Am. Chem. Soc.*, 2011, **133**, 7296–7299.

20498 | *J. Mater. Chem. A*, 2018, **6**, 20491–20499

This journal is © The Royal Society of Chemistry 2018

29 L. Ma, Y. Hu, G. Zhu, R. Chen, T. Chen, H. Lu, Y. Wang, J. Liang, H. Liu, C. Yan, Z. Tie, Z. Jin and J. Liu, *Chem. Mater.*, 2016, **28**, 5733–5742.

30 X. Zheng, J. Xu, K. Yan, H. Wang, Z. Wang and S. Yang, *Chem. Mater.*, 2014, **26**, 2344–2353.

31 Y. H. Chang, C. T. Lin, T. Y. Chen, C. L. Hsu, Y. H. Lee, W. Zhang, K. H. Wei and L. J. Li, *Adv. Mater.*, 2013, **25**, 756–760.

32 K.-C. Pham, Y.-H. Chang, D. S. McPhail, C. Mattevi, A. T. S. Wee and D. H. C. Chua, *ACS Appl. Mater. Interfaces*, 2016, **8**, 5961–5971.

33 D. J. Li, U. N. Maiti, J. Lim, D. S. Choi, W. J. Lee, Y. Oh, G. Y. Lee and S. O. Kim, *Nano Lett.*, 2014, **14**, 1228–1233.

34 X. Li, G. Zhu, Q. Kang, Z.-D. Huang, X. Feng, Y. Li, R. Liu and Y. Ma, *RSC Adv.*, 2015, **5**, 55396–55400.

35 K.-J. Huang, L. Wang, Y.-J. Liu, Y.-M. Liu, H.-B. Wang, T. Gan and L.-L. Wang, *Int. J. Hydrogen Energy*, 2013, **38**, 14027–14034.

36 Y. Zhang, W. Sun, X. Rui, B. Li, T. Tan Hui, G. Guo, S. Madhavi, Y. Zong and Q. Yan, *Small*, 2015, **11**, 3694–3702.

37 M. A. Bissett, I. A. Kinloch and R. A. W. Dryfe, *ACS Appl. Mater. Interfaces*, 2015, **7**, 17388–17398.

38 K. Singh, S. Kumar, K. Agarwal, K. Soni, V. Ramana Gedela and K. Ghosh, *Sci. Rep.*, 2017, **7**, 9458.

39 F. N. I. Sari and J.-M. Ting, *Sci. Rep.*, 2017, **7**, 5999.

40 G. da Silveira Firmiano Edney, C. Rabelo Adriano, J. Dalmaschio Cleocir, N. Pinheiro Antonio, C. Pereira Ernesto, H. Schreiner Wido and R. Leite Edson, *Adv. Energy Mater.*, 2013, **4**, 1301380.

41 W. Zhou, X. Cao, Z. Zeng, W. Shi, Y. Zhu, Q. Yan, H. Liu, J. Wang and H. Zhang, *Energy Environ. Sci.*, 2013, **6**, 2216–2221.

42 H. Wu, X. Lu, G. Zheng and W. Ho Ghim, *Adv. Energy Mater.*, 2018, **8**, 1702704.

43 Y. Dong, Y. Chen, P. Jiang, G. Wang, X. Wu and R. Wu, *RSC Adv.*, 2016, **6**, 7465–7473.

44 H. Wu, J. Geng, P. Han, H. Ge, A. M. Alenizi and G. Zheng, *J. Mater. Chem. A*, 2017, **5**, 23840–23843.

45 J. Zhang, T. Wang, D. Pohl, B. Rellinghaus, R. Dong, S. Liu, X. Zhuang and X. Feng, *Angew. Chem.*, 2016, **128**, 6814–6819.

46 M. Gong, W. Zhou, M.-C. Tsai, J. Zhou, M. Guan, M.-C. Lin, B. Zhang, Y. Hu, D.-Y. Wang, J. Yang, S. J. Pennycook, B.-J. Hwang and H. Dai, *Nat. Commun.*, 2014, **5**, 4695.

47 T. Li, Y. Zuo, X. Lei, N. Li, J. Liu and H. Han, *J. Mater. Chem. A*, 2016, **4**, 8029–8040.

48 X. Chia, N. A. A. Sutrisnoh and M. Pumera, *ACS Appl. Mater. Interfaces*, 2018, **10**, 8702–8711.

49 H. Zhang, H. Jiang, Y. Hu, P. Saha and C. Li, *Mater. Chem. Front.*, 2018, **2**, 1462–1466.

50 D. Gopalakrishnan, D. Damien, B. Li, H. Gullappalli, V. K. Pillai, P. M. Ajayan and M. M. Shaijumon, *Chem. Commun.*, 2015, **51**, 6293–6296.

51 P. Hu, T. Wang, J. Zhao, C. Zhang, J. Ma, H. Du, X. Wang and G. Cui, *ACS Appl. Mater. Interfaces*, 2015, **7**, 26396–26399.

52 D. Merki and X. Hu, *Energy Environ. Sci.*, 2011, **4**, 3878–3888.

53 D. Merki, S. Fierro, H. Vrubel and X. Hu, *Chem. Sci.*, 2011, **2**, 1262–1267.

54 L.-L. Feng, G. Yu, Y. Wu, G.-D. Li, H. Li, Y. Sun, T. Asefa, W. Chen and X. Zou, *J. Am. Chem. Soc.*, 2015, **137**, 14023–14026.

55 N. Mahmood, Y. Yao, J. W. Zhang, L. Pan, X. Zhang and J. J. Zou, *Adv. Sci.*, 2017, **5**, 1700464.

56 R. Subbaraman, D. Tripkovic, D. Strmcnik, K.-C. Chang, M. Uchimura, A. P. Paulikas, V. Stamenkovic and N. M. Markovic, *Science*, 2011, **334**, 1256.

57 G. Yilmaz, X. Lu and G. W. Ho, *Nanoscale*, 2017, **9**, 802–811.

58 H. Tong, W. Bai, S. Yue, Z. Gao, L. Lu, L. Shen, S. Dong, J. Zhu, J. He and X. Zhang, *J. Mater. Chem. A*, 2016, **4**, 11256–11263.

59 Y. Zhang, W. Sun, X. Rui, B. Li, H. T. Tan, G. Guo, S. Madhavi, Y. Zong and Q. Yan, *Small*, 2015, **11**, 3694–3702.